Chapter 11

XAO Analysis – AO's and Their Populations in Crystal Fields

Kiyoaki Tanaka and Yasuyuki Takenaka

Additional information is available at the end of the chapter

http://dx.doi.org/10.5772/50517

1. Introduction

There are two ways to the analysis of electron density distribution (EDD) measured by X-ray diffraction. Multipole refinement (Stewart, 1969, 1973; Hansen & Coppens, 1978) expresses EDD as a linear combination of spherical harmonics. Using the determined functions, EDD is analyzed with Bader topological analysis (Bader, 1994). The concept of critical points of Bader theory defines the characters of chemical bonds. However, it does not give atomic orbital (AO) and its electron population, except for orbitals in high symmetry crystal fields where AO's are defined by theory. The other is based on quantum-mechanical orbital-models and gives the physical quantities just mentioned. The objective of this chapter is to introduce one of the second methods, the X-ray atomic orbital analysis (XAO) (Tanaka et al., 2008; hereinafter referred to as *I*), and its application to metal and rare-earth complexes, where advantages of XAO are revealed quite clear.

XAO is closely related to the electron population analysis (Stewart, 1969; Coppens et al., 1971). However, it was abandoned since the orthonormal relationships between orbital functions caused severe parameter interactions in conventional least-squares refinements. Later, the method incorporating the ortho-normal relationships between AO or MO (molecular orbital) was formulated by employing Lagrange's unknown multiplier method (Tanaka, 1988; hereinafter referred to as *II).*

The AO-based EDD refinement has been started from 3d-transition metal complexes with so high crystal symmetry that the AO's are known by the crystal field theory. Spin states of the metals in perovskites, $KCoF_3$ and $KMnF_3$ (Kijima et al., 1981, 1983) and $KFeF_3$ (Miyata et al., 1983) were determined to be high spin. On the other hand, mixed orbitals of $3d_{x^2-y^2}$ and $3d_{z^2}$ in Jahn-Teller distorted $KCuF_3$ were determined (Tanaka et al., 1979). The hybrid

orbital of $3d_{z^2}$ and 4s of Cu^+ which made O-Cu-O straight bond in $CuAlO_2$ was also determined (Ishiguro et al., 1983). The investigations on $KNiF_3$ and $KCuF_3$ are, to our knowledge, the first ones that determined spin states and AO's by X-ray diffraction, respectively. The Cu^{2+} ion in $[Cu(daco)_2](NO_3)_2$ (daco: diazacyclooctane) is in the crystal field C_i. Five d-orbitals were determined with the least-squares method stated in *II.*

These investigations revealed that the anharmonic vibration (AHV) of atoms could not be ignored, since significant peaks still remained after removing the *3d*-peaks on difference density maps. They were attributed to the AHV of the metal atoms (Tanaka & Marumo, 1982; Ishiguro et al. 1983). For these investigations, a method proposed by Dawson et al., (1967), which had been applied only to high symmetry crystals, was made applicable to atoms in a general crystal field (Tanaka & Marumo, 1983).

Since the ratio of the number of bonding electrons to those in the unit cell becomes smaller as the atomic number increases, very accurate structure factors are necessary for X-ray EDD investigations of rare-earth compounds. Thus, the EDD analysis based on chemical-bond theories had not been done when we started the study on CeB_6. Actually, the ratio in CeB_6 is 1/88, which demands us to measure structure factors with the accuracy less than 1 %. Rare-earth crystals are usually very hard and good resulting in enhanced extinction and multiple diffraction (MD). Therefore, MD was investigated using the method by Tanaka & Saito (1975) in which an effective way to detect MD and correct for it were proposed. It introduced the time-lag between the relevant reflections, which usually do not occur at exactly the same time, to the method by Moon and Shull (1964). The effect of MD was demonstrated through the study of PtP_2 (Tanaka, et al., 1994) by measuring intensities avoiding MD and compared to those measured at the bisecting positions.

The frontier investigations aiming to measure 4f-EDD were done for CeB_6 (Sato, 1985) at 100 and 298 K and for nonaaqualanthanoids (Ln:La, Ce, Pr, Nd, Sm, Eu, Gd, Tb, Dy, Yb and Lu) (Chatterjee at al. 1988). Significant peaks were found around these rare-earth atoms on the residual density maps. However, the aspherical features of 4f-EDD were not analyzed quantitatively by the X-ray scattering factors calculated with AO's in a crystal field. The first *4f*-EDD analysis of CeB_6 with the crystal field model but without spin-orbit interaction exhibited T_{1u} state was occupied (Tanaka et al. 1997). The ground state of the 4f-state was found to be $4f(j=5/2)\Gamma_8$ by the inelastic neutron scattering (Zirngiebl et al., 1984). When the spin-orbit interaction is taken into account, the total sum **J** of the orbital and spin angular momentum **L** and **S**, **J=L+S**, becomes a good quantum number. In the following discussion *J* values of *p*, *d*, *f* orbitals are attached as a subscript on the right-hand side of each orbital. The experiment does not contradict to our results. It was, however, investigated again at 100, 165, 230 and 298 K (Tanaka & Ōnuki, 2002) by introducing the spin-orbit interaction. Our experiments ascertained that *4f* electron occupied $4f_{5/2}\Gamma_8$. orbitals. It revealed further that the electron population of them, $n(4f_{5/2}\Gamma_8)$, decreased on lowering the temperature. $4f_{5/2}\Gamma_8$ electrons are transferred to the B_6 moiety below room temperature. In addition to it just significant amount of $4f_{5/2}\Gamma_7$ electrons were found at 298 K, which was expected to be due to the thermal

excitation. Thus, the electron population above room temperature became very interesting. Since the energy gap between the two $4f_{5/2}$ orbitals is about 500 K, the X-ray intensities were measured at 430 K expecting for $4f_{5/2}\Gamma_7$ to be more populated (Makita et al., 2007). The results were surprising. The $4f_{5/2}\Gamma_7$ is more populated than $4f_{5/2}\Gamma_8$, and $5d_{5/2}\Gamma_8$ is fully occupied at 430 K, which is expected to be at least a few ten thousands degrees higher than the *4f* orbitals. The electron configurations of CeB_6 at 340 and 535 K were further investigated to confirm the results (Makita et al., 2008). The EDD of SmB_6 ($4f^5$) was studied (Funahashi, et al., 2010) below room temperature. $4f_{5/2}\Gamma_8$and $4f_{5/2}\Gamma_7$ orbitals are fully or partially occupied. It is noted that $5d_{5/2}\Gamma_8$ occupation was also found. The physical properties such as electric resistivity are correlated to the electron configuration.

2. Basic formalism of XAO

2.1. AO's in crystal fields

The i-th AO, $\psi_{\alpha,i}(\mathrm{r})$ (i=1,2,...,M) of the α-th atom are expressed with N basisfunctions, $\psi_k(\mathbf{r})$,

$$\psi_{\alpha,i}(r) == \sum_{k}^{N} c_{ik}\psi_k(\mathbf{r}),\ i = 1,2,...,M, \tag{1}$$

where c_{ik} is a constant to be determined in the XAO analysis with the least-squares method incorporating orthonormal relationship between AO's (Tanaka, 1988). Matrices and vectors are written in upper-case letters and bold lower-case letters, and superscript ' means a transposed matrix or a row vector, respectively. The basis functions, $\psi_k(\mathbf{r})$ are listed in Table 1 of *I*. They are expressed using polar coordinate (r, θ, ϕ) as a linear combination of a product of a radial function $R_{nl}(r)$ and a spherical harmonic $Y_{lm_l}(\theta,\phi)$ as,

$$\psi_k(\mathbf{r}) = \sum_{m_l=-l}^{l} d_{k,m_l} R_{nl}(r) Y_{lm_l}(\theta,\phi), \tag{2}$$

where n, l and m_l are principal, azimuthal and magnetic quantum numbers. The non-relativistic radial functions, $R_{nl}(r)$ (Mann, 1968) and relativistic functions calculated by *HEX* (Liberman et al., 1971) were mainly used for the XAO analysis. d_{k,m_l} 's are listed in Table 1 of I. Since approximate c_{ik}'s were necessary at the start of the non-linear least-squares calculation, they were calculated by taking the crystal field, which was calculated by placing a proper point charge on each atom, as a perturbation to the system (Kamimura, et al., 1969). For details, see eqs. (52)-(56) of *I*. The adjustable variables c_{ik}'s in the least-squares calculation are listed for all point group symmetries in Tables 4 and 5 in *I*.

2.2. Least-squares method incorporating ortho-normal condition

In a non-linear least-squares refinement, mathematical and physical relationships between parameters should be taken into account to avoid parameter interaction. The conventional

one used in X-ray crystallography was improved to obtain AO/MO by taking into account the orthonormal relationship between wave functions (Tanaka, 1988),

$$\sum_{m}^{N}\sum_{n}^{N} c_{im}^{*} c_{jn} s_{mn} = \delta_{ij} \tag{3}$$

where $s_{mn} = \int \psi_m^* \psi_n d\mathbf{r}$ and N is the number of basis functions. δ_{ij} is Kronecker's δ. Assuming c_{im}'s are real, it is rewritten with (M,N) matrix $C=\{c_{im}\}$ and (N,N) matrix $S=\{s_{mn}\}$,

$$CSC' = I, \tag{4}$$

where I is the unit matrix of order M. Using Lagrange's unknown multiplier λ_{ij},, the value Q to be minimized in the least-squares method becomes,

$$Q = \mathbf{v}' M_f^{-1} \mathbf{v} - \sum_{i\leq}^{M}\sum_{j}^{M} \lambda_{ij} \left(\sum_{m}^{N}\sum_{n}^{N} c_{im} c_{jn} s_{mn} - \delta_{ij}\right) \tag{5}$$

For definition of $\mathbf{v}$ see eqs. (10a) to (10d) of II. Putting c_{im} as the sum of the true value c_{im}^0 and its small shift Δc_{im}, Q is expressed by ignoring the terms higher than second order of Δc_{im},

$$Q = \mathbf{v}' M_f^{-1} \mathbf{v} - \sum_{i\leq}^{M}\sum_{j}^{M} \lambda_{ij} \left(\sum_{m}^{N}\sum_{n}^{N} (\Delta c_{im} c_{jn}^0 + c_{im}^0 c_{jn}) s_{mn} - \delta_{ij}\right), \tag{6}$$

Putting $\lambda_{ij}'=(1+\delta_{ij})\lambda_{ij}/2$, Q is differentiated to give,

$$\delta Q = 2\boldsymbol{\delta}\mathbf{x}'(A' M_f^{-1} A\mathbf{x} - A' M_f^{-1}\mathbf{f}) - 2\sum_{i}^{M}\sum_{j}^{M} \lambda_{ij}' \sum_{m}^{N}\sum_{n}^{N} \delta(\Delta c_{im} c_{jn}^0 s_{mn}) = 0, \tag{7}$$

where $\mathbf{x}$ represents least-squares estimates of parameters. The first term is obtained following the usual procedure. For $\mathbf{x}$, A and M_f, see Hamilton (1964). After alligning Δc_{im}'s linearly and adding at the end of $\mathbf{x}$ for simplicity, λ_{ij} is expressed in terms of $\boldsymbol{c}_{im}$ by using the orthonormal relationship in eq. (3). Then the final secular equation is obtained,

$$(I-R)A' M_f^{-1} A\mathbf{x} = (I-R)A' M_f^{-1}\mathbf{f}, \tag{8}$$

where I is unit matrix of order P, total number of variables. The (P,P) matrix R is expressed in terms of c_{ik}'s. It makes the inverse matrix of $(I-R)A' M_f^{-1} A$ in (8) calculable. The explicit form of $R=\{r_{ij}\}$ under the limiting conditions (10) for i, j, k and l is,

$$\mathrm{r_{ij}} = \left\{\mathrm{SC'C}\right\}_{\mathrm{kl}}, \tag{9}$$

$$\begin{aligned} &\mathrm{P-MN+(m-1)N+1 \leqq i,j \leqq P-MN+mN,} \\ &\mathrm{k = i-\left\{P-MN+(m-1)N\right\},\ l = j-\left\{P-MN+(m-1)N\right\},} \end{aligned} \tag{10}$$

where m runs from 1 to M. The other elements r_{ij} not defined here are zero.

2.3. Electron density and structure factors

The electron density $\rho_\alpha(\mathbf{r})$ of the αth atom centered at $\mathbf{r}_\alpha^{atom}$ is divided into that of the core and valence orbitals, $\rho_{a,valence}(\mathbf{r})$. It is further expressed from eq. (1),

$$\rho_{\alpha,valence}(\mathbf{r}) = \sum_i n_{\alpha,i}\rho_{\alpha,i}(\kappa_i(\mathbf{r}-\mathbf{r}_\alpha^{atom})) = \sum_i n_{\alpha,i}\Psi^*_{\alpha,i}(\kappa_i(\mathbf{r}-\mathbf{r}_\alpha^{atom}))\Psi_{\alpha,i}(\kappa_i(\mathbf{r}-\mathbf{r}_\alpha^{atom})), \quad (11)$$

where $n_{\alpha,i}$ is the number of electrons of $\Psi_{\alpha,i}$. κ_i expresses the expansion $(\kappa_i > 1)$ or contraction $(\kappa_i > 1)$ of i-th orbital (Coppens et al., 1979). Atom α in the asymmetric unit is translated to $\mathbf{r}_{\alpha\sigma}^{atom}$ by the σ-th crystal symmetry operation. Then the structure factor is,

$$F(\mathbf{k}) = \sum_\alpha \omega_\alpha \sum_\sigma f_{\alpha\sigma}(\mathbf{k})\exp[i\mathbf{k}\cdot\mathbf{r}_{\alpha\sigma}^{atom}]T_{\alpha\sigma}(\mathbf{k}), \quad (12)$$

where $f_{\alpha\sigma}(\mathbf{k})$ is an atomic scattering factor and $\mathbf{k}$ is a scattering vector. The αth atom at $\mathbf{r}_{\alpha\sigma}^{atom}$ is displaced by atomic vibration to $\mathbf{r}_{\alpha\sigma}^{atom} + \mathbf{u}$. It perturbs the periodicity of the crystal and reduces diffracted intensity. Then the atomic displacement parameter (ADP),

$$T_{\alpha\sigma}^{atom}(k) = \left\langle \exp(i\mathbf{k}\cdot\mathbf{u}) \right\rangle, \quad (13)$$

is calculated as an average in space and time of exp(i**k**·**u**) by assuming each atom vibrates independently from each other. $f_{\alpha\sigma}$ is the sum of the scattering factors of core and valence electrons, $f_{\alpha\sigma}^{core}(\mathbf{k})$ and $f_{\alpha\sigma}^{valence}(\mathbf{k})$. $f_{\alpha\sigma}^{valence}(\mathbf{k})$ is expressed as,

$$f_{\alpha\sigma}^{valence}(\mathbf{k}) = \sum_i n_i f_{\alpha,\sigma,i}^{valence}(\mathbf{k}), \quad (14)$$

where n_i is the number of electrons of the ith valence orbitals. $f_{\alpha,\sigma,i}^{valence}(\mathbf{k})$ is a Fourier transform of $\rho_{\alpha,\sigma,i}^{valence}(\mathbf{r})$. Final expression of $f_{\alpha,\sigma,i}^{valence}$ becomes,

$$\begin{aligned} f_{\alpha,\sigma,i}^{valence} &= \sum_k \sum_{k'} c_{ik}^* c_{ik} \sum_{K=|l-l'|}^{l+l'} < j_K > \sum_{M=-K}^{K} i^K \sqrt{2(2K+1)}\Theta_K^M(\beta_\sigma)\exp(iM\gamma_\sigma) \\ &\times \sum_{m_l=-l}^{l} \sum_{m_{l'}=-l'}^{l'} d_{k,m_l}^* d_{k',m_{l'}} c^K(lm_l, l'm_{l'}), \end{aligned} \quad (15)$$

where $K+l+l'$ is even. $M = m_l - m_{l'}$ *and* $|l-l'| \le K \le l+l'$. $\langle j_K \rangle$ is expressed as,

$$\langle j_K \rangle = \int R_{nl}(r)R_{n'l'}(r)j_K(kr)r^2 dr \quad (16)$$

j_K is Bessel function of order K. For $(\beta_\sigma,\gamma_\sigma)$, see Appendix B of *I*.

2.4. Anharmonic vibration (AHV)

Gaussian probability density functions (p.d.f.) of atoms are Fourier transformed to give harmonic ADP. Gram-Charier (G-C) formalism is widely used to introduce AHV. However, it expresses aspherical EDDs both from orbital functions and AHV, as shown clearly by Mallinson et al. (1988). Thus, it may not be adequate for accurate EDD researches. The method based on Boltzmann statistics (Dawson et al. 1967, Willis, 1969) was employed,

$$T_{\alpha\sigma}^{atom}(\mathbf{k}) = \int \exp(-V(\mathbf{u})/k_B T)\exp(i\mathbf{k}\cdot\mathbf{u})d\mathbf{u} \Big/ \int \exp(-V(\mathbf{u})/k_B T)d\mathbf{u}, \tag{17}$$

where k_B is Boltzmann constant, and T is absolute temperature. Assuming each atom vibrates independently and defining $\boldsymbol{u}(u_1,u_2,u_3)$ on the Cartesian coordinates parallel to the principal axes of the thermal ellipsoid of harmonic ADP, potential V(**u**) is expressed as,

$$V(\mathbf{u}) = V_0 + \frac{1}{2}\sum_{i=1}^{3} b_i u_i^2 + \sum_{i,j,k}{}' c_{ijk}u_i u_j u_k + \sum_{i,j,k,l}{}' q_{ijkl}u_i u_j u_k u_l + \ldots\ldots \tag{18}$$

where i, j, k, l run from 1 to 3 and ' means they are permutable. There are 10 cubic and 15 quartic terms. Potential expansion terminates at the quadratic terms in the harmonic ADP.

By assuming the sum of the third and the fourth terms in (18) is much smaller than $k_B T$, b_i, c_{ijk} and q_{ijkl} are introduced into structure factor formalism using (12), (17) and (18).

3. Experimental

3.1. Multiple diffraction (MD)

MD occurs when two or more reflections are on the Ewald sphere. When the incident beam with wave length λ enters parallel to the unit vector **j,** and a primary reflection, the intensity of which is measured, is at the reflecting position, the conditions for a secondary reflection, $h_1h_2h_3$, to occur become as follows (Tanaka & Saito, 1975),

$$\left|\mathbf{e}_3\cdot(\mathbf{j}/\lambda + h_3\mathbf{b}_3\right| \le 1/\lambda \tag{19}$$

$$\left|\mathbf{e}_2\cdot(\mathbf{j}/\lambda + h_2\mathbf{b}_2 + h_3\mathbf{b}_3\right| \le \left[1/\lambda^2 - \left\{\mathbf{e}_3\cdot(\mathbf{j}/\lambda + h_3\mathbf{b}_3\right\}^2\right]^{1/2} \equiv r_3 \tag{20}$$

$$\mathbf{e}_1\cdot(\mathbf{j}/\lambda + h_1\mathbf{b}_1 + h_2\mathbf{b}_2 + h_3\mathbf{b}_3) = \pm\left[r_3^2 - \left\{e_2\bullet(\mathbf{j}/\lambda + h_2\mathbf{b}_2 + h_3\mathbf{b}_3)\right\}^2\right] \tag{21}$$

$\mathbf{b}_1$, $\mathbf{b}_2$, $\mathbf{b}_3$ are reciprocal-lattice vectors when the primary reflection exactly fulfills the reflecting condition and $\mathbf{e}_1$, $\mathbf{e}_2$, $\mathbf{e}_3$ are the unit vectors defined as,

$$\mathbf{e}_3 = \frac{\mathbf{b}_1 \times \mathbf{b}_2}{|\mathbf{b}_1 \times \mathbf{b}_2|}, \mathbf{e}_2 = \frac{\mathbf{e}_3 \times \mathbf{b}_1}{|\mathbf{e}_3 \times \mathbf{b}_1|}, \mathbf{e}_1 = \frac{\mathbf{b}_1}{|\mathbf{b}_1|}. \tag{22}$$

Secondary reflections only around the surface of the Ewald sphere are searched using eqs. (19) to (21). Integers h_3 are selected from (19) and integers h_2 are calculated from (20) for each h_3. Then the value of h_1 is evaluated from eq. (21) for each (h_2, h_3). The point (h_1, h_2, h_3) is judged to be a reciprocal lattice point if h_1 is an integer. The Ewald sphere has width due to the divergence of the incident beam, finite size and mosaicity of the crystal, and wavelength spread. It permits some margin from an integer to h_1.

The change of intensity by MD was first formulated by Moon & Shull (1964). Primary and secondary beams usually come on the Ewald sphere with an angle-lag Δε. Using Δε The formalism was modified for a spherical crystal with a radius r (Tanaka & Saito, 1975),

$$\frac{\Delta I_1}{I_1} = \frac{\sqrt{\pi r^2}}{8} Q_{01} \sum_i \left[-g_{01;0i} \left(\frac{Q_{0i}}{Q_{01}} \right) - g_{01;1i} \left(\frac{Q_{1i}}{Q_{01}} \right) + g_{01;i1} \left(\frac{Q_{0i}}{Q_{01}} \right) \left(\frac{Q_{i1}}{Q_{01}} \right) \right]. \tag{23}$$

Subscripts *'0'*, *'1'* and *'i'* stand for the incident, primary and secondary beams. Q_{mn} is the integrated reflectivity per unit volume of a crystal for the m-th incident beam and n-th diffracted beam (m-n process). It is proportional to the squares of the structure factor. In *i-1* process, for example, a secondary beam i acts as an incident beam and is diffracted along the direction of the primary beam *1*, which enhances the intensity of the primary beam. $g_{ij;mn}$ is a function of $\Delta\varepsilon$, Lorentz and polarization factors of the simultaneous i-j and m-n processes. The polarization factor for a general multi-diffracted process was recently formulated (Tanaka et al., 2010). For $g_{ij;mn}$ see Tanaka & Saito (1975). Since $\Delta I_1/I_1$ depends on the ratio of Q_{mn}'s and Δε of sharp primary and secondary reflections, ΔI_1 fluctuates sharply. Eq. (23) was applied to diformohydrazide (Tanaka, 1978) and two peaks on the N-N bond in the difference density map became one peak at the middle of the bond.

The EDD analyses of compounds with metals and rare-earth elements need accurate measurements of structure factors, however MD affects the measured intensity seriously since Q_{mn} is large. However correction for it does not seem fruitful, since each primary reflection has many secondary reflections and MD depends sharply on crystal orientation and half-width of each Bragg peak. Thus it is better to avoid MD by rotating a crystal around the reciprocal vector of the primary reflection (ψ – rotation) so that secondary reflections move apart from the Ewald sphere and measure at ψ where $\Delta I_1/I_1$ is minimum. For actinoid compounds, MD cannot be avoided and the correction for it becomes necessary.

4. XAO analysis for crystals in the O_h crystal field

4.1. 3d, 4f and 5d orbitals in the O_h crystal field

In the present chapter EDD investigations on the first-transition metal complexes and rare earth compounds in O_h crystal field are mainly stated. Thus it is worth while to represent the

energy level splitting of d- and f-states in Figs.1(a) and (b) (Funahashi, 2010). The spin-orbit splitting is neglected in a strong field model. For $(3d)^n$ systems strong field model is often employed. In $(4f)^n$ and $(5d)^n$ systems the two splittings are of the same order of magnitude. Weak field models are employed for CeB_6 and SmB_6. Their quantization axes point to the face-centre of the cubic unit cell, where no B atom exists. Note that the order of the levels in Fig. 1(a) is inverted, that is, t_{2g} orbitals lies lower than e_g, when ligands are on the quantization axes like $KCoF_3$ (section 4). In weak field *5d*- and *4f*-states split into *j*=3/2 and *j*=5/2 states, and into *j=5/2* and *j=7/2* states by the spin-orbit interaction. The O_h crystal field splits them further. Lobes of $4f_{5/2}\Gamma_8$ extend along <100> directions while those of $4f_{5/2}\Gamma_7$ orbitals along <110> and <111> as illustrated in Fig. 7 of Makita et al. (2007).

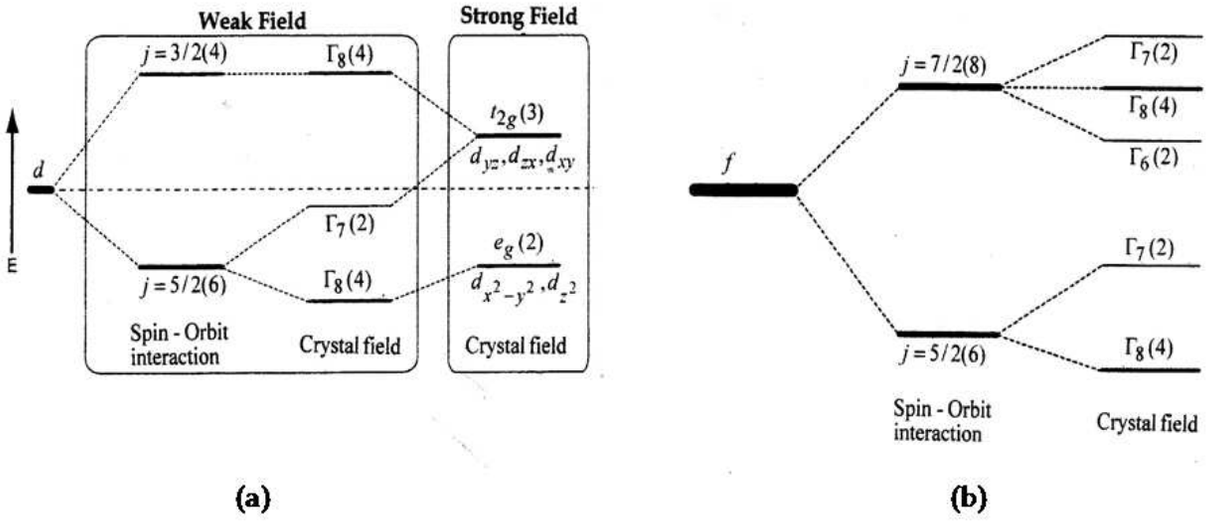

Figure 1. Energy-level splitting of (a) d- and (b) f-states in the O_h crystal field with the degeneracy of each state in parentheses. Each orbital of a strong field can have two electrons.

4.2. *3d*-EDDand spin states in $KCoF_3$, $KMnF_3$ and $KFeF_3$

The peak due to 3d electrons was first reported for $[Co(NH_3)_6][Co(CN)_6]$ (Iwata & Saito, 1975) around the Co atom in $\bar{3}$ crystal field. Later electron distribution at 80 K was reported (Iwata, 1977). *3d*-EDD in γ–Co_2SiO_4 (Marumo et al., 1977) and $CoAl_2O_4$ (Toriumi, et al., 1978) were also observed. The electron density around Co in $KCoF_3$ was first analysed quantitatively based on the *3d*-orbitals in O_h crystal field (Kijima et al., 1981). A crystal was shaped into a sphere of diameter 0.13 mm, and intensities were measured up to 2θ=130°with a four-circle diffractometer using MoKα radiation without avoiding MD. c_{ik}'s in (1) are fixed constants because of the high symmetry as listed in Tables 1(b) and 5(b) of *I*. κ_i in eq. (11) was not introduced to the investigations in sections 4 5.1 and 5.2. Scattering factors of $d_{x^2-y^2}$, d_{z^2}, d_{yz}, d_{zx} *and* d_{xy} orbitals are calculated with eq. (15). When electrons occupy the five *d*-orbitals equally, that is $(t_{2g})^{4.2}(e_g)^{2.8}$ for Co^{2+}, atoms have spherical EDD. Hereinafter the refinement with the spherical scattering factors and without assuming AHV is called as spherical-atom refinement, in which type *I* or *II* anisotropic extinction (Becker &

Coppens, 1974a, b, 1975) was assumed. The difference density map assuming the spherical-atom, high and low spins, $(t_{2g})^5(e_g)^2$ and $(t2g)^6(eg)^1$, are shown in Figs. 2(a) to (c). Peaks remained after spherical-atom refinement were reduced and enhanced after high- and low-spin refinements, respectively. Large and almost no peaks in Fig. 2(c) and Fig. 2(b) demonstrate that Co^{2+} is in the high-spin state. Spin-state was first determined by X-ray diffraction in this study. In the similar way, the spin-states of 3d-transition metals in $KMnF_3$ (Kijima et al., 1983) and $KFeF_3$ (Miyata et al., 1983) were determined to be high-spin.

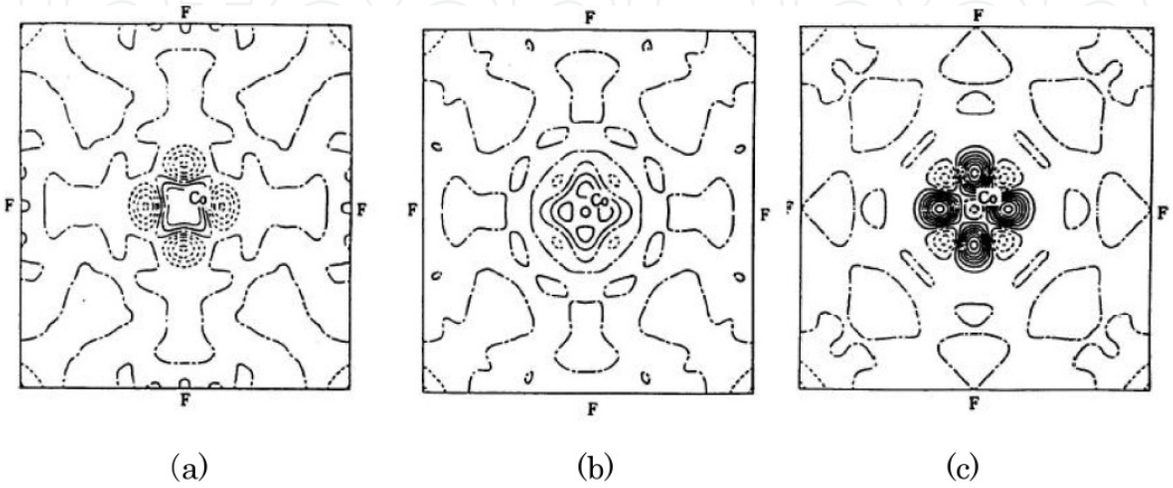

Figure 2. Difference density after refinements of (a) spherical-atom, (b) high-spin, (c) low- spin models. Contours at 0.2 eÅ^{-3}. Negative and zero in broken and dashed-dotted lines.

5. Experimental AO determination

When symmetries of crystal fields are low, c_{ik}'s in (1) become unknown variables, and it is necessary to determine them by the least-squares method keeping the orthonormal relationship between AO's. Independent variables, c_{ik}'s, and the relation between them are listed for 32 point group symmetries in Tables 4 and 5 of *I*.

5.1. Jahn-Teller distortion in $KCuF_3$ and mixed $d_{x^2-y^2}$ and d_{z^2} orbital

In $KCuF_3$ each F^- ion between Cu^{2+} ions ($3d^9$) shifts from the centre by Jahn-Teller effect. It makes short Cu-F_s, medium Cu-F_m, parallel to *c*-axis, and long Cu-F_l bonds, resulting in *mmm* point group symmetry for Cu^{2+}. Difference density after spherical-atom refinement exhibits non-equivalent four holes in Fig. 3 (b) (Tanaka et al. 1979). Table 5(b) of *I* indicates a mixing of $3d_{z^2}$ *and* $3d_{x^2-y^2}$ in the crystal field *mmm*,

$$\begin{aligned}\psi_G &= \cos(\varphi/2)d_{z^2} + \sin(\varphi/2)d_{x^2-y^2},\\ \psi_E &= \sin(\varphi/2)d_{z^2} - \cos(\varphi/2)d_{x^2-y^2}.\end{aligned} \tag{24}$$

The peaks on *Cu-Fl* in Fig. 3(a) correspond to the lone pair of ψ_G. Putting two and one electrons to ψ_G and ψ_E, $cos(\phi/2)$ became 0.964(18). 3d-peaks in Fig. 3 (a) and (b) were

deleted in (c) and (d). It confirms orbitals in eq. (24) are quite reasonable. The orbital functions except the phase factor were determined for the first time from X-ray diffraction experiment. However, significant peaks still remained. The positive and negative peaks along <100> and <110> in Fig.3(c) indicate preferential and inhibitive vibration of Cu^{2+}, respectively. Therefore, AHV of Cu^{2+} was analysed (Tanaka & Marumo, 1982). The obtained potential in (18) corresponds to the peaks and removes them as seen in the residual density in Fig. 4. Our study on AHV started from this investigation. Since the AHV peaks appear in Fig. 3(c) and (d) after the *d*-electron peaks were removed, the aspherical peaks due to electron configuration and vibration of Cu^{2+} seem to be separated well.

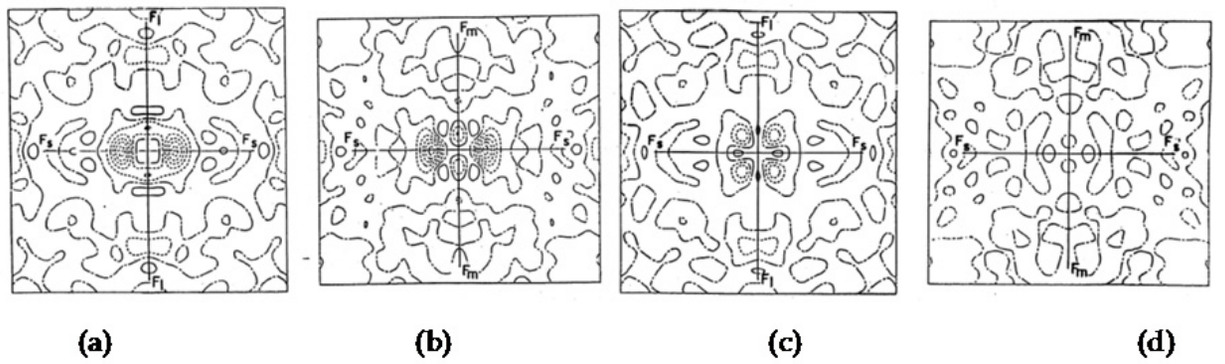

Figure 3. Difference density after spherical-atom refinement on (a) (001) and (b) (220) planes passing Cu^{2+} at (1/2,0,0). That after d-orbital analysis on (c) (001) and (d) (220). Contours are the same as those in Fig. 2.

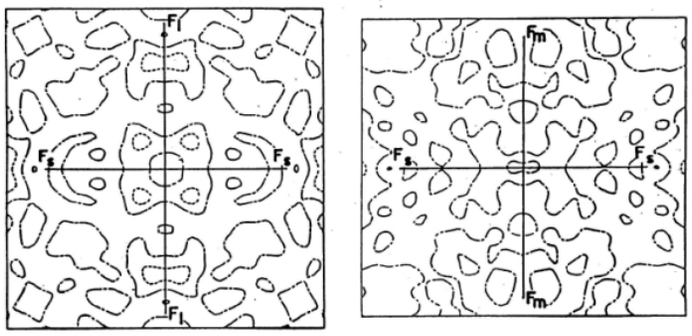

Figure 4. Difference density after AHV analysis. Contours are the same as those in Fig.2.

5.2. 3d orbitals in $\bar{1}$ crystal field of $Cu(daco)_2(NO_3)_2$

The Cu^{2+} ion ($3d^9$) of $Cu(daco)_2(NO_3)_2$(daco: 1,5-diazacyclooctane) is on the centre of symmetry and forms a coordination plane with the four N atoms in daco (Hoshino, et al., 1989). Difference densities on and perpendicular to the Cu-N_4 plane after the spherical-atom refinement are shown in Fig. 5(a) and (b). Negative four peaks in Fig. 5 (a) near Cu^{2+} correspond to a 3d-hole. However, the peaks do not locate on the Cu-N bonds. Since the crystal field of the Cu atom is C_i, d-orbitals of Cu^{2+} are expressed as a linear combination of $d_{x^2-y^2}$, d_{z^2}, d_{yz}, d_{zx} *and* d_{xy} orbitals and all the 25 coefficients c_{ik} were refined with the

method in *II*. Since approximate c_{ik}'s are necessary for the non-linear least-squares refinement, they are calculated putting a point charge on each atom (Kamimura et al., 1969). $\langle j_K \rangle_{3d}$ of Cu^{2+} were taken from International Tables for X-ray crystallography (1974, vol. IV). After each cycle of refinement, new set of coefficients were orthonormalized by the Löwdin's method (Löwdin, 1950). Refinement was converged and the coefficients c_{ik}'s, population n_i and κ_i are listed in Table 1. The number of significant cik's is seven among 25 coefficients. Orbital 1 in Table 1 is the hole orbital. It is not a pure $d_{x^2-y^2}$ but a mixed orbital of $d_{x^2-y^2}$ and d_{zx} orbitals, c_{14}=0.57(59) is not significant. The hole and large negative and positive peaks in Fig. 5 were removed in Fig. 6. Further AHV refinement removed the peaks in Fig.6, but that prior to the d-orbital analysis did not improve Fig. 5.

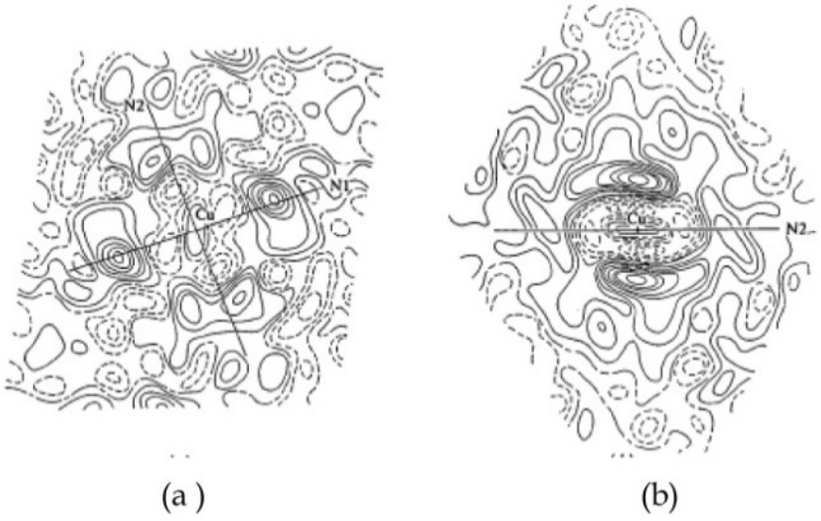

Figure 5. Difference density after spherical-atom refinement on (a) Cu-N_4 plane and (b) the plane perpendicular to it. Contours are the same as those in Fig. 2.

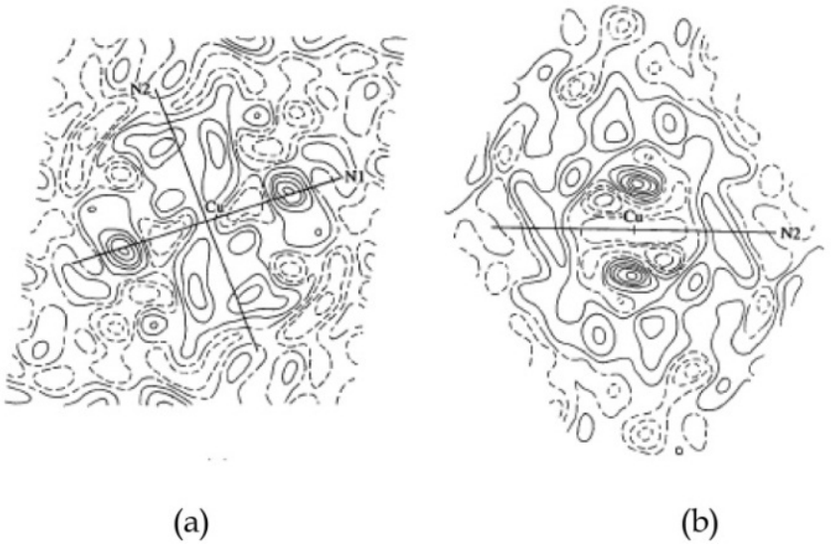

Figure 6. Difference density after 3d-orbital analysis. Contours are the same as in Fig. 2

When G-C formalism was applied to an iron complex, it removed the peaks equally well as the multipole refinement did (Mallinson, et al., 1988). Our AHV analysis is based on the classical thermodynamics and does not have such a problem, though the p.d.f. function $exp[-V(\mathbf{u})/k_BT]$ is not integrable (Scheringer, 1977) at a place far from the nucleus. However, we can apply it safely as long as it is applied within the region where the sum of the third and fourth terms in (18) is much smaller than k_BT. The condition is usually fulfilled in the investigations of EDD.

i	n_i	κ_i	$d_{x^2-y^2}$	d_{z^2}	d_{yz}	d_{zx}	d_{xy}
1	1.0	0.97(11)	**0.75(34)**	0.21(59)	0.23(216)	0.57(59)	0.10(79)
2	2.0	1.37(7)	0.08(28)	0.12(17)	–0.19(19)	0.10(26)	**–0.97(6)**
3	2.0	0.81(5)	**0.63(22)**	–0.15(52)	–0.44(44)	**–0.61(34)**	0.06(22)
4	2.0	0.71(4)	0.04(32)	**–0.93(13)**	–0.10(29)	0.34(41)	–0.06(10)
5	2.0	0.90(5)	0.15(76)	–0.22(45)	**0.84(43)**	–0.42(85)	**–0.22(15)**

Table 1. 3d-orbital parameters c_{ik}'s of Cu^{2+}. Significant ones in thick lines

6. 4f-EDD in rare-earth hexa-borides

4f-EDD analysis has become more and more important since many rare-earth compounds with interesting physical properties, such as high-temperature super conductors, have been found. The EDD of rare-earth hexa-borides were investigated since they are famous for their properties related to the Kondo effect.

6.1. XAO analysis of CeB_6

Ce and B atoms are at the body-centre and on the edges of the cubic unit cell with the B_6 regular octahedra at the corners as shown in Fig. 7. Ce is in an O_h crystal field and B atoms are on 4-fold axes. CeB_6 is a typical dense Kondo material with Kondo-temperature T_k=2 K. The magnetic moment decreases with that of temperature and vanishes below T_K. However, Kondo effect starts above room temperature (Ōnuki et al. 1984). Thus, change of EDD below room temperature is interesting although our diffractometer did not permit to measure below 2K. Intensities were measured at 100, 165, 230 and 298 K aiming to separate the two kinds of asphericity of EDD stated in 5.1 and 5.2 (Tanaka & Ōnuki, 2002). MD was avoided by ψ–scan with the program *IUANGL* (Tanaka et al., 1994). Crystal was shaped into a sphere with a radius 36 μm to reduce absorption, extinction and MD.

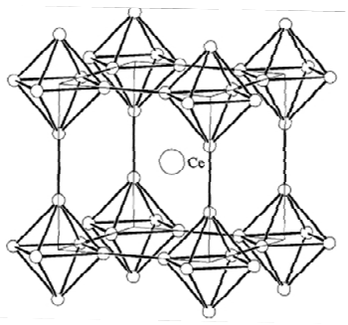

Figure 7. Crystal structure of CeB_6

Spin-orbit interaction was introduced into the XAO analysis. Four-fold degenerate $4f_{5/2}\Gamma_8$ orbitals were taken from Table 4 (b) of *I* as,

$$\Psi_1^{4f} = \sqrt{\frac{5}{6}}\psi_1 + \sqrt{\frac{1}{6}}\psi_5, \Psi_2^{4f} = \sqrt{\frac{1}{6}}\psi_2 + \sqrt{\frac{5}{6}}\psi_6, \Psi_3^{4f} = \psi_3, \Psi_4^{4f} = \psi_4, \tag{25}$$

where ψ_i (i=1 to 6) are basis functions in Table 1(c) of *I*. In the similar way $5p_{1/2}$, $5p_{3/2}$ and $4f_{5/2}\Gamma_7$ and $4f_{7/2}\Gamma_6, \Gamma_7, \Gamma_8$ orbitals were introduced into the XAO analysis.

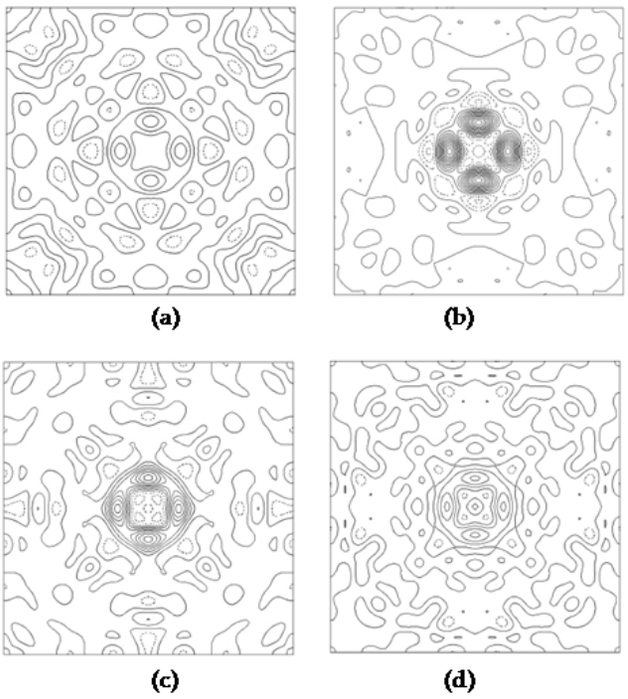

Figure 8. Difference density on (100) plane around Ce at (a) 100 K, (b) 165 K, (c) 230 K, (d) 298 K. Contours are the same as those in Fig. 2.

Temp.	*Ce*	$n(\Gamma_8)^*$	$\kappa(\Gamma_8)$	$\kappa(5p_{3/2})$	q_{1111}	q_{1122}	*B*	$n(2p_x)$	$n(2p_z)$	$\kappa(2p_x)$	$\kappa(2p_z)$	*Ce – B*
100*K*		13(1)	179(8)	95(2)	47(19)	–131(48)		27(6)	103(8)	93(31)	92(12)	3.0416(3)
165*K*		15(2)	158(12)	98(2)	–14(6)	39(15)		52(4)	52(8)	85(16)	108(11)	3.0440(4)
230*K*		19(2)	157(11)	100(2)	0(4)	–1(11)		69(4)	16(8)	51(19)	130(18)	3.0459(7)
298*K*		21(2)	160(10)	100(2)	6(2)	–13(5)		67(4)	19(8)	54(17)	130(13)	3.0439(4)

Table 2. Orbital and AHV parameters. n(X), and κ(X) are a number of electrons and κ of the orbital X. n(x10^{-2}), κ (x10^{-2}), q_{iijj} (x10^{-19} J$Å^{-4}$). $5p_{3/2,1/2}$ and *2s* are fully occupied. $n(2p_x)=n(2p_y)$ and $\kappa(2p_x)=\kappa(2p_y)$. Unit of Ce-B is Å. *:n(Γ_7) is 4.2(3.6)x10^{-2} only at 298 K.

6.1.1. XAO analysis of CeB_6 below room temperature

After spherical-atom refinement for ions, Ce^{3+} and $B^{0.5-}$, the populations of the orbitals were refined keeping the sum of them equal to that of nuclear charges. When populations of them exceeded one/two or became negative, they were fixed to one/two or zero. In our program

QNTAO (Tanaka, 2000) each sub-shell is treated as an pseudo-atom sharing atomic parameters with the other sub-shells. It enables us to analyze the EDD of non-stoichiometric atoms, since valence electrons can be treated independently from the core electrons. Basis functions in Table 1 of *I* are automatically assigned to each AO labelled with *2l+1* and the number of basis functions. Since high symmetry fixes c_{ik}'s in (1), the other orbital parameters and atomic parameters, including AHV were refined. Electron density around Ce on (001) after spherical-atom refinement is shown in Fig. 8. The peak heights around Ce increase from *0.6, 1.2 to 2.0 eÅ*$^{-3}$on lowering the temperature to 165 K and reduce to *0.6* eÅ^{-3} at *100 K*. After XAO analysis they were removed, exhibiting they were due to the *4f*-electrons. Parameters of AO's and AHV are listed in Table 2. No electrons were found in $4f_{7/2}$ orbitals but B-*2s* and Ce-*5p* are always fully occupied. $n(4f_{5/2}\Gamma_7)$ has value 0.042(36) only at 298 K but $4f_{5/2}\Gamma_8$ is occupied at the four temperatures. It agrees with the previous experiments (Zirngiebl et al., 1984;Sato et al., 1984). Shorter Ce-B at 298 K than that at 230 K seems to be correlated to $4f_{5/2}\Gamma_7$. It extends along $\langle 111 \rangle$ or to the centre of B_6 octahedron making them extend to reduce electrostatic repulsion. Expanded $2p_x$ still has electrons. Total number of *4f*-elctrons mainly composed of $4f_{5/2}\Gamma_8$ are 0.98(11), 0.77(8), 0.61(7) and 0.52(6) at 298, 230, 165 and 100 K. They decrease with temperature. Table 2 tells $2p_{x,y}$ and *4f* electrons are transferred to $2p_z$, main contributor to the shortest covalent B-B bonds between B_6 octahedra (called as B-B_{out}).

Electron accumulation at *B-*B_{out} enhances q_{1111} and q_{1122} of Ce at 165 K. They change signs and become more larger at 100 K. Negative and positive q_{1111} at 165 K and 100K indicates that vibration of Ce at body-centre to the face-centre is favorable at 165 K, and becomes unfavorable at 100 K. This is the reason for the enhanced peak in Fig. 8(b) and reduced one in (a). Negative q_{1122} at 100 K indicates the attractive force to the edge centre increased by the accumulated $2p_z$ electrons. Since sum of the mean radii of B-*2p* and Ce-*5p* in free space, 2.2048+1.7947=3.9995 Å (Mann, 1968) is longer than Ce-B distance in Table 2, a slight expansion/contraction of them affects the potential seriously. Since the 5p orbitals are fully occupied, EDD's of them are spherical. B-$2p_x$ is closer than $2p_z$ to the spherically distributed Ce-$5p_{3/2}$ electrons. $\kappa(5p_{3/2})$ exhibits slight expansion on lowering the temperature. Expansion and contraction of $5p_{3/2}$and $4f_{5/2}\Gamma_7$ in Table 2 reduces the potential of *4f* orbitals lying closer to the nucleus. However, it contradicts to the decrease of *4f* population. It indicates that the system resists against losing *4f* electrons from Ce by making the potential of Ce more stable. It reminds us of the Le Chatelier's law: the system resists against the change. Then why are *4f* electrons allowed to flow out of Ce in spite of the reduced potential energy of the Γ_8 state? The enhanced AHV at 165 and 100 K produced new ways of vibration along $\langle 100 \rangle$ and $\langle 110 \rangle$ directions increasing the ways to attain the energy of the system. Therefore, the enhanced AHV at lower temperatures means an increase in entropy. Since the electron transfer itself from Ce to $(B\text{-}B)_{out}$ increases entropy, it cannot be stopped.

The XAO analysis of CeB_6 was applied to the weak-field model. The crystal structure, EDD, electron populations, expansion/contraction parameters and AHV parameters were quite consistent with each other at different temperatures. Therefore, the 4f-EDD is concluded to be measured and analyzed successfully.

6.1.2. 4f population inversion and fully occupied 5d states at 430 K

The electron population at 298 K exhibited slightly occupied $4f_{5/2}\Gamma_7$. Since the energy gap between $4f_{5/2}\Gamma_8$ and Γ_7 was reported to be 530-560 K (Loewenhaupt et al., 1985; Zirngiebl et al., 1984), XAO analysis at 430 K was performed to observe more electrons in Γ_7 (Makita et al., 2007). For details of the high-temperature diffraction equipment, see PhD thesis of Makita (Makita, 2008). Scattering factors of Ce were evaluated from relativistic AO's calculated by the program *GRASP* (Dyall et al., 1989). Difference density around Ce on (001) after the spherical-atom refinement is shown in Fig. 9(a). The 4f-peaks closest to Ce elongate along <110> in contrast to those below room temperature in Fig. 8. They are surrounded by the four peaks of 0.65 eÅ^{-3}, which extend along <100>, and disappeared after the analysis of the 4f peaks. However, the population of $4f_{5/2}\Gamma_8$ and Γ_7 were 0.06(3) and 0.36(11). Higher temperature reverses the populations of $4f_{5/2}\Gamma_8$ and Γ_7. The peaks outside the *4f*-peaks, called *5d* peaks, remained almost unchanged. Accordingly $5d_{5/2}\Gamma_7$ and Γ_8 orbitals were further refined. The population of $5d_{5/2}\Gamma_8$, $n(5d_{5/2}\Gamma_8)$, exceeded 1.0 and was fixed. $n(4f_{5/2}\Gamma_8, \Gamma_7)$ and $n(5d_{5/2}\Gamma_8)$ were 0.06(2), 0.37(1) and 1.0, while $5d_{5/2}\Gamma_7$ was vacant. R factor was reduced from 1.25 to 1.16 %. The peaks outside the *4f* peaks reduced slightly from 0.65 to 0.59 eÅ^{-3} in Fig. 10(b). Since *5d* orbitals extend in a large area, in contrast to 4f orbitals, slight change of EDD is significant. Thus electron densities around *5d*–peaks in Figs. 9 (a) and (b) were numerically integrated to give 3.41 and 1.57 electrons. XAO analysis explained 54 % of the *5d*-peaks. Therefore $d_{5/2}\Gamma_8$ is concluded to be occupied, though peaks still remained. It may be ascribed to the inaccurate *5d-AO*'s (Claiser et al., 2004).

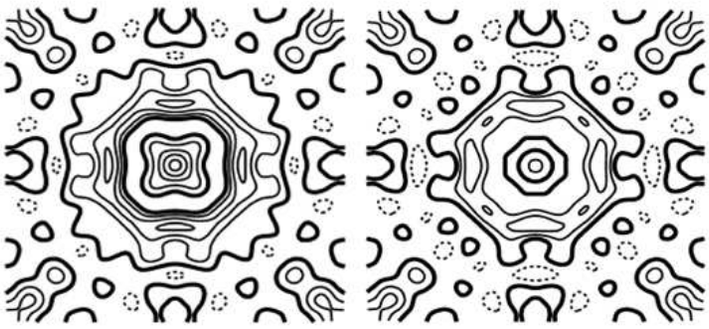

Figure 9. Differnece density around Ce at 430 K on (100) after (a) spherical-atom refinement and (b) final residual density. Contours at 0.2 eÅ^{-3}. Negative and zero contours in dotted and thick lines.

Why are *5d* orbitals occupied? The energy level of the Ce-*5d* and B-*2p* calculated by Liberman et al., (1971) and Mann (1967) are -0.63 and -0.62 a.u. They are very close compared to the Ce-4f level at -0.75 a.u. Thus B-2p electrons are transferred to 5d levels predominantly according to the first-order perturbation theory. The radial distribution functions of the relevant AO's are illustrated in Fig. 10. Putting the origin of B at r=3.045 Å, *2p* was drawn to the reverse side. *5d* and *2p* overlap well, and it is expected that *2p* electrons which distribute all over the crystal through the network of B-B covalent bonds can be transferred most probably to *5d* orbitals. Electrons traveling in the crystal are expected to stay at $5d_{5/2}\Gamma_8$ orbitals when they come close to Ce.

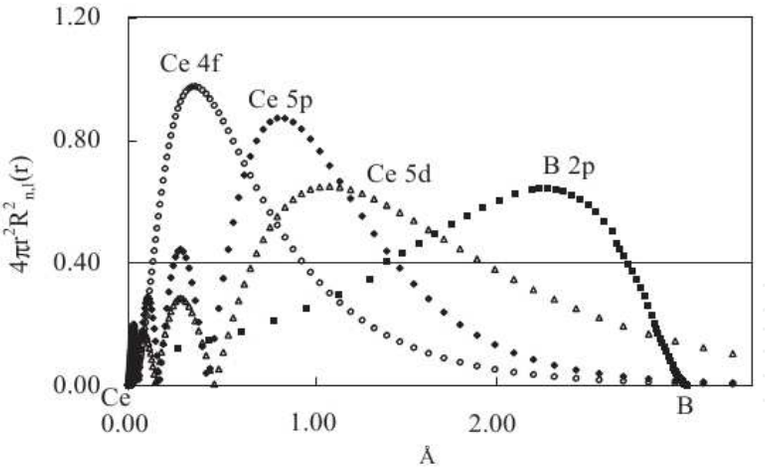

Figure 10. Radial distribution functions of Ca and B.

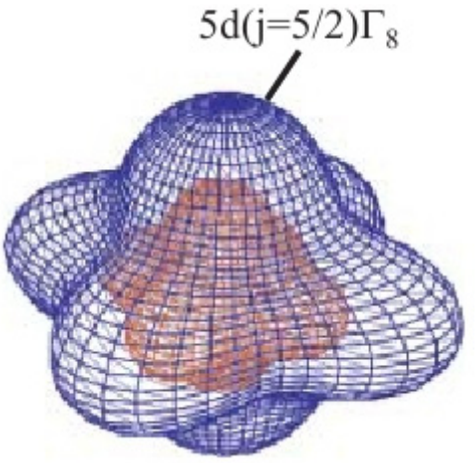

Figure 11. $4f_{5/2}\Gamma_8$ (red) and $5d_{5/2}\Gamma_8$ obritals.

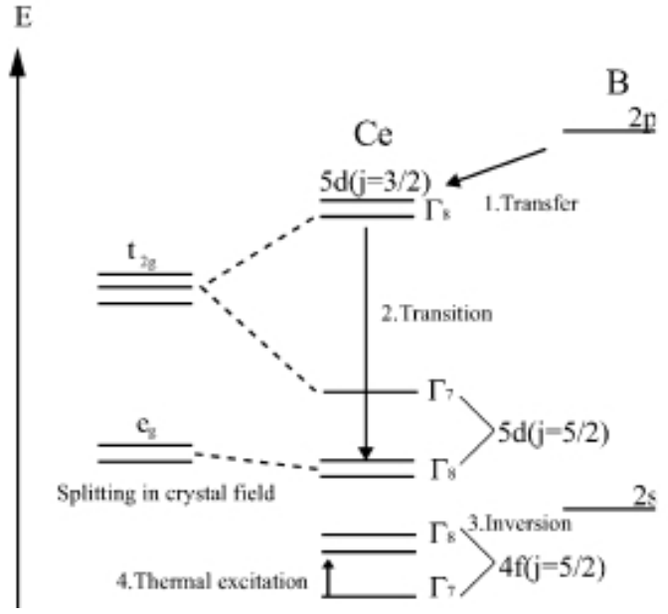

Figure 12. 5d- and 4f-energy levels expected from the electron populations.

Why does $4f_{5/2}\Gamma_8$-Γ_7 inversion occur? $5d_{5/2}\Gamma_8$ orbitals are located outside of $4f_{5/2}\Gamma_8$ having exactly the same symmetry (Fig. 11). Since $5d_{5/2}\Gamma_8$ is fully occupied, the potential of the $4f_{5/2}\Gamma_8$ orbital is enhanced. It is the reason for the population inversion of $4f_{5/2}\Gamma_8$ and Γ_7. The energy level diagram expected from the electron populations obtained by the XAO analysis is shown in Fig.12. Since the quantization axes are defined parallel to <100>, T_{2g} states locate higher than E_g. $5d_{3/2}\Gamma_8$ orbital closely related to T_{2g} is located highest among the 5d orbitals as shown in Fig. 12. From the populations obtained, 2p electrons seem to be transferred to $5d_{5/2}\Gamma_8$ orbitals, directly or first to $5d_{3/2}\Gamma_8$ and then to $5d_{5/2}\Gamma_8$.

6.1.3. Electron configuration at 340 and 535 K

In order to confirm the *5d*-occupation in CeB_6 at 430 K, XAO analyses were done at 340 and 535 K. The difference densities, as well as electron configurations, are different from each other as shown in Fig. 13. Since the electrons are continually transferred between *2p* and *5d* orbitals, the crystal field seems to change with temperature resulting in different directions of the 4f and 5d peaks in Fig. 13. However, it is confirmed that *5d* orbitals in CeB_6 are occupied above room temperature (Makita et al., 2008).

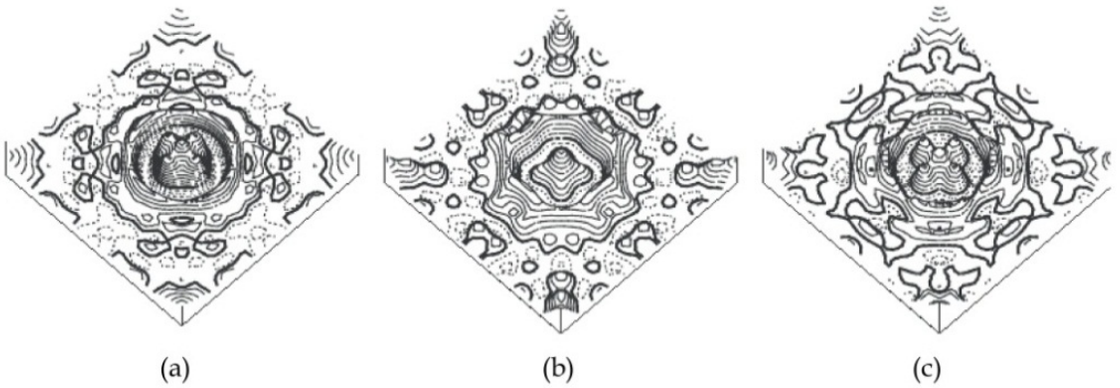

Figure 13. Bird-eye view of difference densities around Ce at (a) 340, (b) 430 and (c) 535 K. Contours as in Fig. 9 except the interval of 0.1 eÅ^{-3}. Frames are parallel to <100>axes.

6.2. XAO analysis of SmB_6

SmB_6 formally has five 4f electrons. In order to extend XAO analysis to multi 4f-electron system, EDD of SmB_6 was measured at 100, 165, 230 and 298 K (Funahashi, et al., 2010). It is interesting to see how physical properties as a Kondo insulator are explained by the XAO analysis. The shadow in the difference density at 230 K in Fig. 14 specifies roughly the area of *5d* peaks. $5p_{3/2}$, $4f_{5/2}\Gamma_8$,Γ_7 and AHV were refined reducing the *4f* peaks in Fig. 14(a). However, since *4f*-peaks still remained along <100>, the populations of $4f_{7/2}\Gamma_6$,Γ_7,Γ_8 were refined but only Γ_6 orbital which extends along <100> more sharply than $4f_{5/2}\Gamma_8$ survived. Since peaks (peak A) remained in the *5d*-area, $5d_{5/2}\Gamma_8$,Γ_7 and $5d_{3/2}\Gamma_8$ were added in the refinement and only $5d_{5/2}\Gamma_8$ orbital, which stems from e_g orbital of the storing field model had population. Fig. 14(b) exhibits that peak A is reduced from 0.43 to 0.17 eÅ^{-3} and 4f-peaks are almost deleted. Final parameters are listed in Table 3.

The electron configuration in Table 3 is correlated to the physical properties of SmB_6 as follows: (a) SmB_6 is a Kondo insulator. Its electric resistivity increases gradually like semiconductors below room temperature and begins to increase steeply below 30 K with a decrease in temperature. It also begins to increase like metals above room temperature (Ueda & Onuki, 1998). *2p* and $5d_{3/2}\Gamma_8$ orbitals consist of the conduction band (Kimura et al., 1990). Since B-$2p_z$ extends along the edge, it does not overlap with $5d_{3/2}\Gamma_8$ effectively and does not seem to contribute to the band. The population of $2p_x$ in Table 3 as well as the resistivity steadily increases on lowering temperature. n($5d_{5/2}\Gamma_8$) also increases from 230 K. The increase of populations indicates that of localized electrons. It may be correlated to the increase of the resistivity. (b) $4f_{7/2}\Gamma_6$ are vacant only at 100 K, although they are occupied at the other three temperatures. It may be correlated to the band gap between the *4f* states, which is reported to start developing between 150 and 100 K (Souma, et al., 2002). (c) Among the *5d* orbitals only the $5d_{5/2}\Gamma_8$ are occupied. Since $5d_{5/2}\Gamma_8$ orbitals correspond to e_g in the strong field model as illustrated in Fig. 1, it agrees with the band calculation of LaB_6 by Harima (1988), reporting that *5d*-e_g and *2p* of B consist of the conduction band.

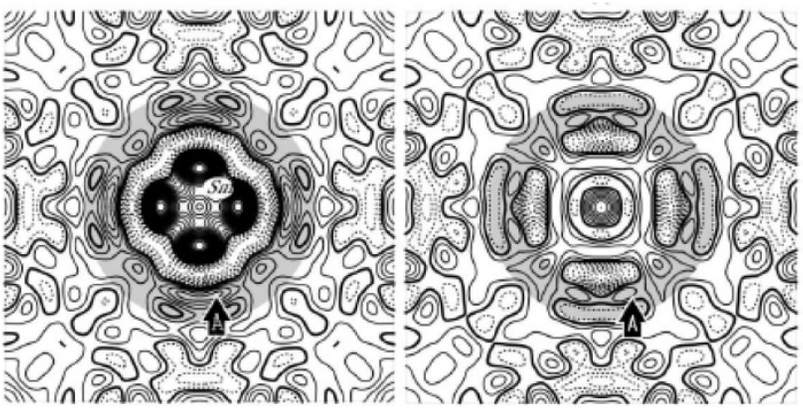

(a) (b)

Figure 14. Difference density at 230 K after (a)spherical-atom refinement and (b) XAO analysis. Contours as in Fig. 13.

	$n(4f_{5/2}\Gamma_8)$	$n(4f_{5/2}\Gamma_7)$	$n(4f_{7/2}\Gamma_6)$	$n(5d_{5/2}\Gamma_8)$	$n(2p_x)$	$n(2p_z)$
100*K*	0.96(9)	0.48(12)	0.0	1.0	0.21(8)	0..45(17)
165*K*	1.0	0.67(13)	0.44(12)	0.75(24)	0.16(13)	0.55(39)
230*K*	1.0	0.61(13)	0.59(13)	0.56(16)	0.13(7)	0.66(28)
298*K*	0.77(3)	0.59(7)	0.47(6)	0.78(6)	0.07(3)	0.81(12)

Table 3. Temperature dependence of electron populations of Sm *4f*, *5d* and B *2p* orbitals.

7. Bright future for X-ray crystallography

EDD investigation was limited up to 3*d*-transition-metal complexes. However, XAO analysis made EDD investigations of rare-earth compounds as well as non-stoichiometric ones possible. Its application to organic compounds can be attained when it is developed to X-ray

molecular orbital analysis (XMO). Since the least-squares method stated in 2.2 was formulated for MO models, XMO analysis will be accomplished in a near future. When actinoid compounds become our targets, however, MD-effect is expected to be so much that the avoidance of it by $\psi-$ rotation is impossible and the correction for it will be inevitable.

CeB_6 is a possible quantum-material to emit UV light when electrons in $5d_{5/2}\Gamma_8$ could be transferred to $4f_{5/2}\Gamma_8$, as the investigation at 430 K revealed. The d-f transition is a permitted one by quantum mechanics. Since the 5d-occupation is found in the ground state of CeB_6, some external force is necessary to make the transition occur. A electron populations in CeB_6 and SmB_6 found by the XAO analysis demostrate the importance of the EDD analysis based on quantum-mechanical orbitals.

As discussed in 5.3, the aspherical properties of EDD and AHV are separated better by the method based on classical Boltzmann statistics than the G-C method. However, recent development of neutron diffraction will make it possible to get intrinsic ADP's and use them as known parameters in X-ray EDD analyses. It will improve XAO analysis of rare-earth complexes and makes the XMO analysis surer and easier.

The accuracy of X-ray structure-factor measurements has been improved so much that every crystallographer will investigate EDD easily as a part of their X-ray structure analysis. The top-up operation with constant incident beam intensity at SR facilities has improved the accuracy of the structure factor measurements from 1 % to 0.1 %. Future of X-ray diffraction is bright.

Author details

Kiyoaki Tanaka and Yasuyuki Takenaka
Nagoya Institute of Technology, Hokkaido University of Education, Japan

8. References

Bader, R. F. W. (1994). Atoms in molecules A quantum theory, Clarendon Press, Oxford, Great Britain

Becker, P. J. & Coppens, P. (1974a). Extinction within the limit of Darwin transfer equations. I. General formalisms for primary and secondary extinction and their application to spherical crystals. *Acta Cryst*. A30, 129-147.

Becker, P. J. & Coppens, P. (1974b). Extinction within the limit of Darwin transfer equations. II. Refinement of extinction in spherical crystals of SrF_2 and LiF. *Acta Cryst*. A30, 148-153.

Becker, P. & Coppens, P. (1975). Extinction within the limit of Darwin transfer equations. III.Non-soherical crystals and anisotropy of extinction. *Acta Cryst*. A31, 417-425.

Chatterjee, A., Maslen, E. N. & Watson, K. J. (1988). Electron densities in crystals of nonaaqualanthanoid(III) tris(trifluoromethanesulfonates). *Acta Cryst*. B44, 386-395.

Claiser, N., Souhassou, M. & Lecomte, C. (2004). Problems in experimental charge modeling of rare *earth* atom complexes: the case of gadolinium. *J. Phys. Chem. Solids*, 65, 1927-1933.

Coppens, P., Guru Row, T. N.., Leung, P., Stevens, E. D., Becker, P. J. & Yang, Y. W. (1979). Net atomic charges and molecular dipole moments from spherical-atom X-ray refinements, and the relation between atomic charge and shape. *Acta Cryst.* A35, 63-72

Coppens, P., Willoughby, T. V. and Csonka L. N. (1971). Electron population analysis of accurate diffraction data. I. Formalisms and restrictions, *Acta Cryst*. A27, 248-256.

Dawson, B., Hurley, A. C. & Maslen V. W. (1967). Anharmonic vibration in fluorite structures. *Proc. Roy. Soc. London Ser. A,* 298, 255-263.

Dyall, K. D., Grant, I. P., Johnson, C. T., Parpia, F. A. & Plummer, E. P. (1989). GRASP* A general-purpose relativistic atomic structure program. *Comput. Phys. Commun*. 55, 425-456.

Funahashi, S. (2010). XAO(X-ray atomic orbital) analysis of the EDD of rare-earth compounds and their physical properties, PhD thesis, Grad. School of Sci. & Eng. Nagoya Inst. of Tech.

Funahashi, S., Tanaka, K. & Iga, F. (2010). X-ray atomic orbital analysis of 4f and 5d electron configuration of SmB_6 at 100, 165, 230 and 298 K. *Acta Cryst*. B66, 292-306.

Hamilton, W. C. (1964). *Statistics in physical science,* The Ronald press company, New, York.

Hansen, N. K. & Coppens, P. (1978). *Testing aspherical atom refinement on small-molecule data sets, Acta Cryst*. A34, 909-921.

Harima, H. (1988). *Theoretical study of the Fermi surface of the rare-earth compounds*, PhD thesis, Tohoku Univ. Japan.

Hoshino, N., Fukuda, Y., Sone, K., Tanaka, K. & Marumo, F. (1989). Single-Crystal X-ray and Optical Studies on Bis(1,5-diazacyclooctane)Copper(II) Nitrate, a thermochromic copper(II) complex involving hydrogen bonds between the ligand and the counter Ion, *Bull. Chem. Soc. Jpn*., 62, 1822-1828.

Ishiguro, T., Ishizaa, N., Mizutani, M., Kato, M., Tanaka, K. & Marumo, F. (1983). Charge-density distribution in crystals of $CuAlO_2$ with d-s hybridization. *Acta Cryst.* B39, 564-569.

Iwata, M. (1977). X-ray determination of the electron density distribution in crystals of $[Co(NH_3)_6][Co(CN)_6]$, *Acta Cryst.* B33, 59-69.

Iwata, M. & Saito, Y. (1973), The crystal structure of Hexaamminecobalt(III) Hexacyanocobaltate(III): an accurate determination, *Acta Cryst*. B29, 822-832.

Kamimura, H., Sugano, S. & Tanabe, Y. (1969). *Ligand field theory and its application*, Tokyo, Syōkabō.

Kijima, N., Tanaka, K. & Marumo, F. (1981). Electron density distribution in crystals of potassium trifluorocobaltate(II), *Acta Cryst*. B37, 545-548

Kijima, N., Tanaka, K. & Marumo, F. (1983). Electron density distribution in crystals of $KMnF_3$ and $KNiF_3$, *Acta Cryst*. B37, 545-548

Kijima, K., Tanaka, K. & Marumo, F. (1983), Electron density distribution in crystals of potassium trifluorocobaltate(II). *Acta Cryst*. B39, 557-561

Kimura, S., Nanba, T., Kunii, S. & Kasuya, T. (1990). Interband optical spectra of rare-earth hexaborides. *J. Phys. Soc. Jpn*, 59 3388-3392.

Liberman, D. A., Cromer, D. T. & Waber, J. T. (1971). Relativistic self-consistent field program for atoms and ions. *Comput. Phys. Commun*. 2, 107-113.

Lowenhaupt, M., Carpenter, J. M. & Loong, C. –K. (1985). Magnetic excitations in CeB_6. *J. Magn. Magn. Mater.* 52, 245-249. (1971).

Löwdin, P. O. (1950). On the nonorthogonality problem connected with the use of atomic wave functions in the theory of molecules and crystals. *J. Chem. Phys*. 18, 365-375.

Makita, R. (2008). Investigation on the physical properties of heavy-atom compounds by X-ray analysis of electron density, PhD thesis. Grad. School of Mat. Sci. & Eng., Nagoya Inst. Tech.

Makita, R., Tanaka, K., Ōnuki, Y. & Tatewaki, H. (2007). Inversion of 4f-states in CeB_6 thermally excited at 430 K, *Acta Cryst*. B63, 683-692.

Makita, R., Tanaka, K., Ōnuki, Y. (2008). 5d and 4f configuration of CeB6 at 340 and 535 K, *Acta Cryst*. B64, 534-549.

Mallinson, P. R., Koritsanszky, T., Elkaim, E., Li, N. & Coppens, P. (1988). The Gram-Charlier and multipole expansions in accurate X-ray diffraction studies. Can they be distinguished? Acta Cryst. A44, 336-342.

Mann, J. B. (1968). Atomic structure calculations II. Hartree-Fock wavefunctions and radial expectation values: Hydrogen to Lawrencium. *Report LA3691. Los Alamos NatioFnal Laboratory*, New Mexico, USA.

Marumo, F., Isobe, M. & Akimoto, S. (1977). Electron-density distribution in crystals of γ-Fe_2SiO_4 and γ-Co_2SiO_4. *Acta Cryst*. B33, 713-716.

Miyata, N., Tanaka, K. & Marumo, F. (1983). Electron density distribution in crystals of iron(II) potassium trifluoride, *Acta Cryst*. B39, 561-564.

Moon, R. M. & Shull, C. G. (1964). The effect of simultaneous reflections on single-crystal neutron diffraction intensities. *Acta Cryst.* 17, 805-812.

Ōnuki, Y., Furukawa, Y. & Komatsubara, T. (1984). Dense Kondo behavior in $Ce_xLa_{1-x}Al_2$. *J. Phys. Soc. Jpn*., 53, 2734-2740.

Sato, S. (1985). Aspherical charge distribution in a crystal of CeB_6. *J. Magn. Magn. Mater*. 52, 310-312.

Scheringer, C. (1977). On the interpretation of anisotropic temperature factors. III. Anharmonic motions. *Acta Cryst*. A33, 879-884.

Souma, S., Kumigashira, H., Ito, T., Takahashi, T. & Kunii, S. (2992). Direct observation of pseudogap of SmB6 using ultrahigh-resolution photoemission spectroscopy. *Physica B*, 312-313, 329-330.

Stewart, R. F. (1969).Generalized XRay scattering factors, *J. Chem. Phys*. 51, 4569-4577.

Stewart, R. F. (1969). Electron population analysis with generalized xray scattering factors: higher multipoles. *J. Chem. Phys*. 51, 4569-4577.

Tanaka, K. (1978). Electron density distribution in crystals of diformohydrazide, *Acta Cryst*. B34, 2487-2494.

Tanaka, K. (1988). X-ray analysis of wavefunctions by the least-squares method incorporating orthonormality. I. General formalism, *Acta Cryst*. A44, 1002-1008.

Tanaka, K. (1993). X-ray analysis of wavefunctions by the least-squares method incorporating orthonormality. II. Ground state of the Cu^{2+} ion of bis(1,5-diazacyclooctane)copper(II) nitrate in a low-symmetry crystal field. *Acta Cryst*. B49, 1001-1010.

Tanaka, K., Kato, Y. & Ōnuki, Y. (1997). 4f-electron density distribution in crystalso of CeB_6 at 165 K and its analysis based on the crystal field theory. *Acta Cryst*. B53, 143-152.

Tanaka, K., Konishi, M. & Marumo, F. (1979). Electron-density distribution in crystals of $KCuF_3$ with Jahn-Teller distortion. *Acta Cryst*. B35, 1303-1308.

Tanaka, K., Kumazawa, S., Tsubokawa, M., Maruno, S. & Shirotani, I. (1994). The multiple-diffraction effect in accurate structure factor measurements of PtP_2 crystals. *Acta Cryst*. A50, 246-252.

Tanaka, K., Makita, R., Funahashi, S., Komori, T. & Zaw Win (2008). X-ray atomic orbital analysis. I. Quantum-mechanical and crystallographic framework of the method. *Acta Cryst*. A64, 437-449.

Tanaka, K. & Marumo, F. (1982). Electron-density distribution and anharmonic vibration in crystals of potassium trifluorocuprate(II). *Acta Cryst.* B38, 1422-1427.

Tanaka, K. & Marumo, F. (1983). Willis formalism of anharmonic temperature factors for a general potential and its application in the least-squares method. *Acta Cryst.* A39, 631-641.

Tanaka, K. & Ōnuki, Y. (2002). Observation of the 4f-electron transfer from Ce to B_6 in the Kondo crystal CeB_6 and its mechanism by multi-temperature X-ray diffraction. *Acta Cryst*. B58, 423-436.

Tanaka, K. & Saito Y. (1975). Simultaneous reflection: Its detection and correction for intensity perturbation. *Acta Cryst.* A31, 841-845.

Tanaka, K., Takenaka, Y., Funahashi, S., Sakakura, T. & Komori, T. (2010). A general expression of the polarization factor for multi-diffraction processes, *Acta Cryst*. A66, 438-440.

Tanaka, K., Tsubokawa, M., Maruno, S. & Shirotani, I. (1994), The multiple-diffraction effect in accurate structure-factor measurements of PtP_2 crystals. *Acta Cryst.* A50, 246-252.

Toriumi, K., Ozima, M., Akaogi, M. & Saito, Y. (1978). Electron-density distribution in crystals of $CoAl_2O_4$. *Acta Cryst*. B34, 1093-1096.

Ueda, K. & Onuki, Y. (1998). *Physics of heavy electron systems*, p. 224, Shokabo, Tokyo.

Willis, B. T. M. (1969). Lattice vibrations and the accurate determination of structure factors for the elastic scattering of X-rays and neutrons. Acta Cryst. A25, 277-300.

Zirngiebl, E., Hillerbrands, B., Blumenröder, S., Güntherrodt, G., Lowenhaupt, M., Carpenter, J. M., Winzer, L. & Fisl, Z.,(1984). Crystal-field excitation in CeB_6 studied by Raman and neutron spectroscopy. *Phys. Rev. B*. 30, 4052-4054.